

See discussions, stats, and author profiles for this publication at: <https://www.researchgate.net/publication/257935471>

# Mixed iron–manganese oxide nanoparticles

ARTICLE *in* THE JOURNAL OF PHYSICAL CHEMISTRY B · SEPTEMBER 2004

Impact Factor: 3.3 · DOI: 10.1021/jp049913

---

CITATIONS

6

---

READS

44

9 AUTHORS, INCLUDING:



Jriuan Lai

University of Washington Seattle

22 PUBLICATIONS 463 CITATIONS

SEE PROFILE



Katja Loos

University of Groningen

146 PUBLICATIONS 2,279 CITATIONS

SEE PROFILE



Min-Hui Cui

Yeshiva University

20 PUBLICATIONS 305 CITATIONS

SEE PROFILE



Thomas Vogt

University of South Carolina

360 PUBLICATIONS 9,225 CITATIONS

SEE PROFILE

## Mixed Iron–Manganese Oxide Nanoparticles

Jruiyan Lai,<sup>†,‡</sup> Kurikka V. P. M. Shafi,<sup>†,‡</sup> Abraham Ulman,<sup>\*,†,‡</sup> Katja Loos,<sup>†,‡</sup> Nan-Loh Yang,<sup>§,‡</sup> Min-Hui Cui,<sup>§,‡</sup> Thomas Vogt,<sup>||</sup> Claude Estournès,<sup>⊥</sup> and Dave C. Locke<sup>#</sup>

Department of Chemical Engineering, Chemistry & Material Science, Polytechnic University, 6 Metrotech Center, Brooklyn, New York 11201, Department of Chemistry, CUNY at Staten Island, 2800 Victory Boulevard, Staten Island, New York, Physics Department and Center for Functional Nanomaterials, Brookhaven National Laboratory, P.O. Box 5000, Upton, New York 11973-5000, UMR7504 CNRS-ULP, Institut de Physique et Chimie des Matériaux de Strasbourg, Cedex, France, The NSF MRSEC for Polymers at Engineered Interfaces, and Department of Chemistry and Biochemistry, CUNY Queens College, 60-30 Kissena Boulevard, Remsen 206, Flushing, New York 11367

Received: January 7, 2004; In Final Form: April 14, 2004

Designing nanoparticles for practical applications requires knowledge and control of how their desired properties relate to their composition and structure. Here, we present a detailed systematic study of mixed iron–manganese oxide nanoparticles, showing that ultrasonication provides the high-energy reaction conditions required for complete atomic level mixing of Fe(III) and Mn(III) when amorphous Fe<sub>2</sub>O<sub>3</sub> nanoparticles are irradiated in the presence of Mn<sub>2</sub>(CO)<sub>10</sub> in ambient atmosphere. X-ray diffraction (XRD) results reveal that the crystal structure of manganese iron mixed oxide nanoparticles changes from spinel to bixbyite with increasing of Mn(III) content. The results of room-temperature magnetization curves are consistent with the XRD patterns and spin density from electron paramagnetic resonance measurements, showing samples converting from superparamagnetic to antiferromagnetic, when the crystal structures of these samples transform from spinel to bixbyite.

### Introduction

Confinement and quantum size effects in nanoparticles induce properties that are significantly different from those of the bulk material as a result of their reduced dimensions.<sup>1</sup> Because of these unique properties, nanomaterials have become a focus of research in modern technology. For example, semiconductor nanoparticles (quantum dots) exhibit discrete energy bands and size-dependent band gap energies; conducting nanoparticles exhibit large optical polarizabilities and nonlinear electrical conductance; and ferromagnetic nanoparticles become superparamagnetic, with size-dependent magnetic susceptibilities.<sup>2–7</sup> However, studies on magnetic nanoparticles are scant compared to, say, those on semiconductor nanoparticles.

Magnetic nanoparticles have applications in information storage,<sup>8</sup> color imaging,<sup>9</sup> magnetic refrigeration,<sup>10</sup> bioprocessing,<sup>11</sup> medical diagnosis,<sup>12,13</sup> and controlled drug delivery<sup>14</sup> and as ferrofluids.<sup>15</sup> Thus, developing new synthetic routes for magnetic nanoparticles and the investigation of their properties are of great importance.<sup>16</sup>

Ferrites, the transition metal oxides having a spinel structure, are used in magnetic inks<sup>17</sup> and magnetic fluids<sup>18</sup> and for the fabrication of magnetic cores of read/write heads for high-speed digital tapes or for disk recording.<sup>19</sup> One important example is the electrically conductive manganese oxide, which stores electrical charge by a double insertion of electrons and cations

into the solid state.<sup>20</sup> Maghemite [ $\gamma$ -Fe<sub>2</sub>O<sub>3</sub>, the ferrimagnetic cubic form of iron(III) oxide] is being used widely for the production of magnetic materials and in catalysis. Because of the small coercivity of Fe<sub>2</sub>O<sub>3</sub> nanoparticles, they can be used as magneto-optical devices. In this paper, we discuss the magnetic properties of sonochemically synthesized mixed iron–manganese oxide nanoparticles.

Various methods have been reported for the synthesis of metal oxide nanoparticles, such as wet chemical,<sup>20,21</sup> electrochemical,<sup>22</sup> and pyrolysis<sup>23,24</sup> techniques, sol–gel reactions,<sup>25,26</sup> and chemical oxidation in micellar media<sup>27</sup> or in polymer<sup>28,29</sup> or mineral matrices.<sup>30,31</sup> The wet chemical methods include coprecipitation,<sup>32–34</sup> spray drying,<sup>35</sup> and hydrothermal processes.<sup>36</sup> The conventional high-temperature ceramic method for the preparation of ferrites can result in the loss of their fine particle nature. The fine ferrite particles are also produced by grinding coarse powders of high-purity bulk material in the presence of kerosene and oleic acid (an organic surfactant).<sup>37</sup> Surfactant nanostructures (reverse micelles) have also been used to synthesize nanosized ferrite particles.<sup>38–40</sup>

Chemists are accustomed to thinking in terms of activation energy. However, in acoustic cavitation, where temperatures in the excess of 5000 K and pressures of 800 atm are produced,<sup>41–43</sup> activation energy becomes meaningless, and chemical reactions can take place that otherwise are impossible. As a result, using ultrasonication, one can achieve mixing at the atomic level of the constituent ions in the amorphous phase so that the crystalline phase can be obtained by annealing at relatively low temperatures.<sup>44</sup> Sonochemistry has been used to prepare various kinds of nanostructured amorphous magnetic materials.<sup>45–52</sup>

\* To whom correspondence should be addressed. E-mail: aulman@duke.poly.edu.

<sup>†</sup> Polytechnic University.

<sup>‡</sup> The NSF MRSEC for Polymers at Engineered Interfaces.

<sup>§</sup> CUNY at Staten Island.

<sup>||</sup> Brookhaven National Laboratory.

<sup>⊥</sup> Institut de Physique et Chimie des Matériaux de Strasbourg.

<sup>#</sup> CUNY Queens College.

## Experimental Section

Iron pentacarbonyl,  $\text{Fe}(\text{CO})_5$  (Aldrich), manganese carbonyl,  $\text{Mn}_2(\text{CO})_{10}$  (98%, Strem), decahydronaphthalene (anhydrous 99+%, Aldrich), and pentane (98% Aldrich) were used as received.

**Synthesis of Amorphous  $\text{Fe}_2\text{O}_3$ .** A total of 4 mL of  $\text{Fe}(\text{CO})_5$  and 40 mL of decahydronaphthalene were mixed in a 100-mL Suslick cell and irradiated with a high-intensity ultrasonic horn (Sonics and Materials with VC-600, 0.5-in. Ti horn, 20 kHz, 100 W/cm<sup>2</sup>) under air, for 3 h. The cell was immersed in an acetone bath (−70 °C) continuously, giving a temperature of about 0 °C inside. The resulting product was centrifuged, washed thoroughly with dry pentane, and dried under a vacuum.

**Synthesis of  $\text{Mn}_2\text{O}_3$ .** The amorphous  $\text{Mn}_2\text{O}_3$  was prepared as above by sonicating 0.5 g of  $\text{Mn}_2(\text{CO})_{10}$  and 40 mL of decahydronaphthalene for 2 h. The resulting brownish solid was then centrifuged, washed, and dried under a vacuum.

**Synthesis of Manganese Iron Mixed Oxide.** The amorphous mixed oxide nanoparticles were prepared by ultrasonication of the stoichiometric amount of amorphous  $\text{Fe}_2\text{O}_3$  and  $\text{Mn}_2(\text{CO})_{10}$  in 40 mL of decahydronaphthalene for 2 h. The resulting product was centrifuged, washed, and dried as above. Crystalline nanoparticles were prepared by annealing the as-prepared amorphous particles at 500 °C for 180 min under an air atmosphere.

**X-ray Diffraction (XRD).** Powder XRD was performed by using a Philips X-ray diffractometer, XRG 3100, equipped with a graphite monochromator mounted near the receiving slit, Cu K $\alpha$  radiation (40 kV, 20 mA,  $\lambda = 1.5418$  Å), and a variable divergence slit. Scans were made from 15 to 75° 2 $\theta$  with a constant step width of 0.01° and a speed of 0.008°/s. XRD samples were prepared by coating them with several drops of nitrocellulose in amyl acetate (concentration 1%) on a quartz plate.

**Synchrotron Powder XRD.** Experiments were performed at the beamline X7A of the National Synchrotron Light Source at Brookhaven National Laboratory with a linear position-sensitive detector gating electronically on the Kr-escape peak.<sup>53</sup> The monochromatic X-rays were obtained using a water-cooled  $\text{Ge}^{111}$  channel cut monochromator. The instrumental resolution in this setup,  $d/d$ , is  $\sim 10^{-3}$ . The sample was contained in an unsealed 0.3-mm capillary, which was rotated at a frequency of roughly 1 Hz to reduce preferred sample orientation effects.

**Transmission Electron Microscopy (TEM).** Nanoparticle size and morphology were determined on a Phillips CM-12 transmission electron microscope (100 keV). Nanoparticles (in toluene) were deposited onto a carbon stabilized Formvar coated copper grid (400 mesh) and allowed to dry.

**Atomic Absorption Spectroscopy (AAS).** Elemental analysis was performed by using Perkin-Elmer flame and graphite furnace AAS. Samples for analysis were predissolved in 37% hydrochloric acid and diluted with 2% nitric acid until the concentration was 5 ppm.

**Magnetic Measurements.** Magnetic data of the solid samples were collected with a Princeton Applied Research vibrating sample magnetometer model 155 (VSM) and a Quantum Design SQUID MPMS-XL (alternating current and direct current modes and maximum static field of  $\pm 5$  T) both in liquid helium and room temperatures. The temperature dependence of the magnetization was measured in the range 5–400 K in an applied field of 20 Oe, after cooling in zero magnetic field (zero-field-cooled, ZFC) or by cooling in a field of 20 Oe (field-cooled, FC).

**Mössbauer Spectroscopy.** Mössbauer measurements were performed using a constant acceleration HALDER-type spectrometer with a room-temperature <sup>57</sup>Co source (Rh matrix) in transmission geometry. The polycrystalline absorbers containing about 10 mg cm<sup>−2</sup> of iron were used to avoid the experimental widening of the peaks. The spectra at 4.2 and 293 K were recorded using a variable-temperature cryostat. The velocity was calibrated using pure iron metal as the standard material. The refinement of the Mössbauer spectra showed an important and abnormal widening of the peaks so that the spectra have been fitted assuming a distribution either of quadrupolar splittings or of hyperfine fields.

**Electron Paramagnetic Resonance (EPR) Spectroscopy.** X-band EPR spectra were recorded on a Bruker ESP380E spectrometer equipped with a HP 5361 frequency counter. The spectra were obtained using the following parameters: microwave power of  $\sim 0.7$  mW, modulation amplitude of 1.045 G, modulation frequency of 100 kHz, time constant of 1.28 ms, sweep time up to 168 s, sweep width of 5000 G, and X axis resolution of 4 K. The unpaired spin density was evaluated by comparison with a diphenylpicrylhydrazyl (DPPH) as an internal standard marker calibrated against  $\text{Mn}^{2+}/\text{CaO}$  with a known spin number. The  $g$  value at room temperature was estimated by the comparison with DPPH. The EPR spectrum was recorded at various temperatures from 140 to 320 K to gather information of the temperature effect on the EPR signal. The  $g$  value in the variable temperature experiment was calculated from magnetic field ( $H$ ) and frequency ( $\nu$ ) that was recorded on a HP 5361B pulse/CW microwave counter.

## Results and Discussion

The report that when  $\gamma\text{-Fe}_2\text{O}_3$  nanoparticles are doped with Mn(III) the transition from the cubic to the more stable hexagonal  $\alpha\text{-Fe}_2\text{O}_3$  structure is suppressed<sup>54</sup> is fascinating, in that it raises the possibility that more thermally stable magnetic nanoparticles can be prepared, simply by adding small quantities of other ions. It was suggested that the suppression of the  $\gamma$ - (cubic) to  $\alpha\text{-Fe}_2\text{O}_3$  (hexagonal) transition is due to the fact that while Mn(III) has a cubic spinel phase (with more free volume) it does not transform into a hexagonal one and, therefore, doping  $\text{Fe}_2\text{O}_3$  with Mn(III) increases the activation energy for the transition to the more compact  $\alpha$  phase, which requires lattice contraction. These ideas trigger further questions such as the following: What happens in higher concentrations of Mn(III)? Can  $\text{Fe}_2\text{O}_3$  and  $\text{Mn}_2\text{O}_3$  mix in any composition? What happens when  $\text{Mn}_2\text{O}_3$  is the majority oxide? Can  $\text{MnFe}_2\text{O}_4$  and  $\text{FeMnO}_4$  be prepared by this route? These questions are not unique to the Fe(III)/Mn(III) mixed oxide system because we have observed the same suppression of the  $\gamma$ - to  $\alpha\text{-Fe}_2\text{O}_3$  for  $\gamma\text{-Fe}_2\text{O}_3$  doped with Co(III). Therefore, to address these intriguing questions we have undertaken detailed systematic studies of mixed Fe(III)–Mn(III) oxides.

While the focus of this paper is the preparation of mixed Fe(III)–Mn(III) oxides and the study of their physical properties, we emphasize that the catalytic function of Mn(III) in mediated oxidations/free radical reactions has been extensively documented.<sup>55</sup> The size of the Mn(III) containing oxide nanoparticles from the synthesis reported here is 1 order of magnitude smaller than the spinel oxide nanoparticles, including  $\text{Mn}_2\text{O}_3$ , reported recently.<sup>44</sup> It is expected that these nanoparticles would have catalytic properties, and as a result of their large surface area, they are expected to be excellent candidates for efficient magnetic separation and retrieval. Our recent paper on the

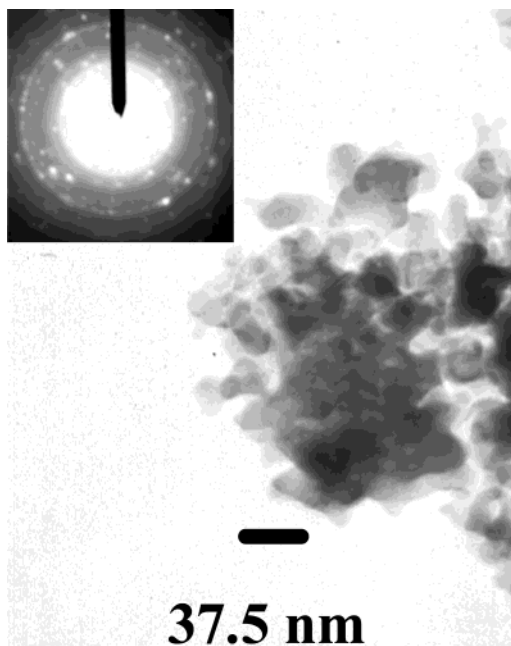


**Figure 1.** TEM images of manganese iron mixed oxide with 44% Mn(III).

enzyme-functionalized magnetic nanoparticles is an excellent example of separation technology using magnetic nanoparticles.<sup>56</sup>

Amorphous manganese iron mixed oxide nanoparticles were prepared by ultrasonication of the stoichiometric mixtures of as-prepared  $\text{Fe}_2\text{O}_3$  amorphous nanoparticles (5–10 nm size in diameter) and  $\text{Mn}_2(\text{CO})_{10}$ . The corresponding crystalline samples were prepared by annealing the nanoparticles at temperatures determined by differential scanning calorimetry measurements. Thus,  $\gamma\text{-Fe}_2\text{O}_3$  nanoparticles were prepared by heating amorphous  $\text{Fe}_2\text{O}_3$  nanoparticles at 300 °C for 3 h, while  $\alpha\text{-Fe}_2\text{O}_3$ ,  $\text{Mn}_2\text{O}_3$ , and manganese–iron mixed oxides were prepared by heating the corresponding samples at 500 °C for 3 h. Figure 1 shows a TEM bright-field image of a representative sample ( $\text{Mn}_{0.44}\text{Fe}_{0.56}\text{O}_3$ ). The image shows aggregation due to sintering, which is a common phenomenon when amorphous nanoparticles are annealed. The selected-area electron diffraction pattern (Figure 1, inset) reveals that these nanoparticles are highly crystalline.

XRD patterns for  $\gamma\text{-Fe}_2\text{O}_3$ , as well for the manganese–iron mixed oxide nanoparticle samples, are presented in Figure 2. As observed previously,<sup>54</sup> the XRD pattern of synthesized  $\text{Fe}_2\text{O}_3$  particles (pattern a) matches well with the standard JSPDS pattern for  $\gamma\text{-Fe}_2\text{O}_3$ . Patterns b–e show the XRD for manganese–iron mixed oxide nanoparticles with Mn(III) atomic concentrations from 12 to 44%. The positions and relative intensities of the strong peaks in patterns b–e match those of the cubic spinel  $\gamma\text{-Fe}_2\text{O}_3$  structure. On the other hand, the synchrotron powder XRD of a sample with  $\leq 5\%$  Mn(III) substitution, prepared under the same conditions, that is, annealing at 500 °C for 3 h, reveals a hexagonal  $\alpha\text{-Fe}_2\text{O}_3$  structure (Figure 3). These nanoparticles represent the first region in the mixed oxide phase diagram, that is to say, when  $\text{Fe}_2\text{O}_3$  is the majority oxide.

Turning to the other end of the composition range, that is, when  $\text{Mn}_2\text{O}_3$  is the majority oxide, Figure 4 shows the XRD patterns of the manganese–iron mixed oxides with Mn(III) concentrations from 78 to 89 atom % (patterns a–c) as well the pure  $\text{Mn}_2\text{O}_3$  (d). Also included is the reported index of the  $\text{Mn}_{2-x}\text{Fe}_x\text{O}_3$  pattern for comparison. The index of  $\text{Mn}_{2-x}\text{Fe}_x\text{O}_3$  is almost the same as that of  $\text{Mn}_2\text{O}_3$ , and, hence, the latter was

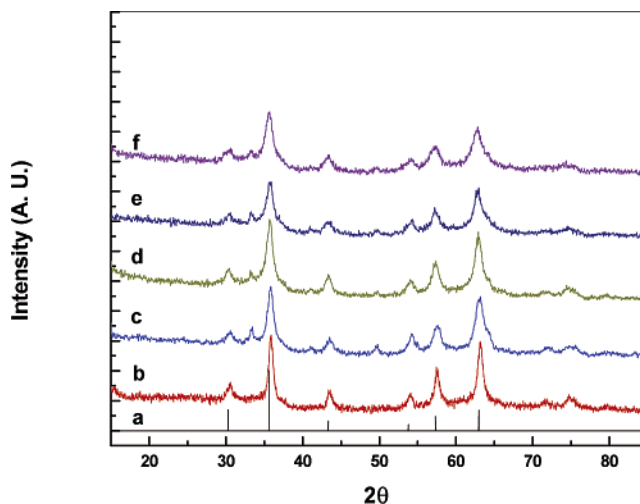


**Figure 2.** XRD patterns: (a) index of  $\gamma\text{-Fe}_2\text{O}_3$ ; (b)  $\gamma\text{-Fe}_2\text{O}_3$ ; (c) 12% Mn(III); (d) 25% Mn(III); (e) 36% Mn(III); and (f) 44% Mn(III).

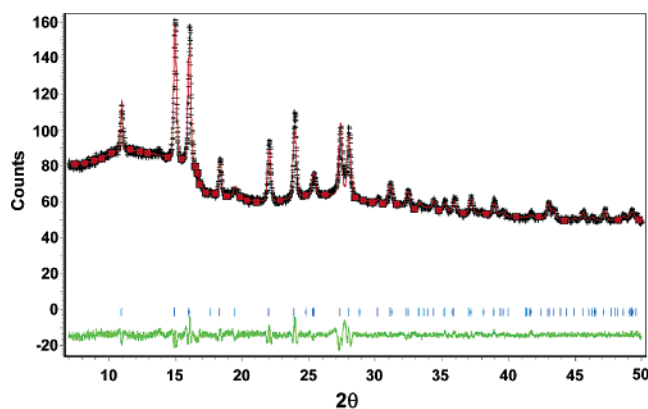


**Figure 3.** Synchrotron powder XRD of sample with  $\leq 5\%$  Mn.

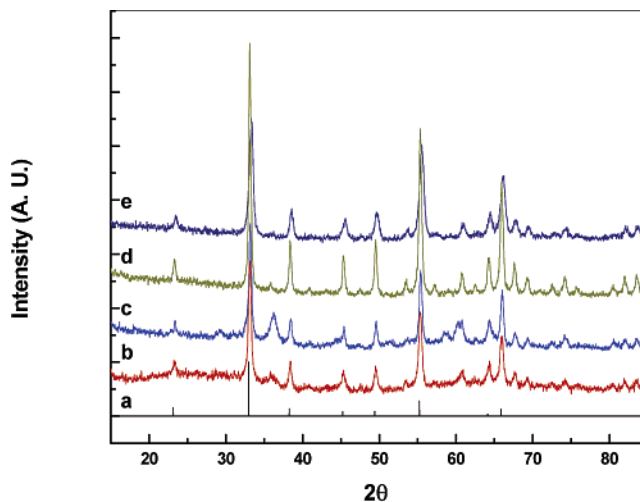


**Figure 4.** XRD patterns: (a) index of  $\text{Mn}_{2-x}\text{Fe}_x\text{O}_3$ ; (b) 78% Mn(III); (c) 81% Mn(III); (d) 89% Mn(III); and (e)  $\text{Mn}_2\text{O}_3$ .

used as the index for both  $\text{Mn}_{2-x}\text{Fe}_x\text{O}_3$  and  $\text{Mn}_2\text{O}_3$  samples. The XRD pattern of the synthesized  $\text{Mn}_2\text{O}_3$  matches with the known pattern of  $\text{Mn}_2\text{O}_3$ . The mixed oxides show the  $\text{Mn}_{2-x}\text{Fe}_x\text{O}_3$  pattern, which is a bixbyite structure.

Interestingly,  $\text{Fe}_2\text{O}_3$  and  $\text{Mn}_2\text{O}_3$  do not mixed in all compositions. Indeed, patterns of samples with 52 and 65% Mn(III) (b and c, respectively, Figure 5) are a mixture of two phases,  $\gamma\text{-Fe}_2\text{O}_3$  (a) and  $\text{Mn}_{2-x}\text{Fe}_x\text{O}_3$  (d), indicating phase separation. This clearly suggests a concentration window where the samples



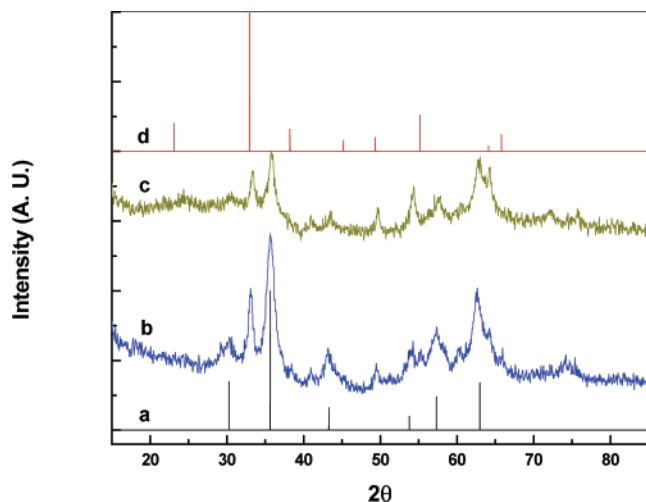


**Figure 5.** XRD patterns: (a) index of  $\gamma\text{-Fe}_2\text{O}_3$ ; (b) 52% Mn(III); (c) 65% Mn(III); and (d) index of  $\text{Mn}_{2-x}\text{Fe}_x\text{O}_3$ .

cannot exist as a single phase. We note that  $\text{MnFe}_2\text{O}_4$  was not detected in any of the samples.

As we have reported earlier for mixed oxides with 8.5% Mn(III) concentration,<sup>54</sup> X-ray studies reveal that, for samples with Mn(III) concentration between 12% and 44 atom %, the transition from spinel ( $\gamma\text{-Fe}_2\text{O}_3$ ) to hematite ( $\alpha\text{-Fe}_2\text{O}_3$ ) is also suppressed. That the mixed oxide samples crystallized as the  $\gamma\text{-Fe}_2\text{O}_3$  phase suggests that these are single-phase compounds and can be best represented as  $(\text{Mn}_x\text{Fe}_{1-x})_2\text{O}_3$ , where  $x = 0.12\text{--}0.89$  or  $\text{Fe}_{2-x}\text{Mn}_x\text{O}_3$  where  $x = 0.24\text{--}0.88$ . If the samples were a physical mixture, the XRD patterns should have peaks of both  $\alpha\text{-Fe}_2\text{O}_3$  and  $\text{Mn}_2\text{O}_3$ , which was not observed in any of the samples.

These single-phase nanoparticles confirm that ultrasonication provides the high-energy environment necessary for complete mixing at the atomic level. Hence, in heterogeneous cavitation, when cavities containing  $\text{Mn}_2(\text{CO})_{10}$  collapse on the solid  $\text{Fe}_2\text{O}_3$  surface, Mn(III) ions are forced into the iron oxide network, thus, replacing some Fe(III) ions. That is to say, the Mn(III) ions occupy “Fe sites” and behave as Fe(III) ions. This is not surprising because the ionic charge and radii of high-spin Fe(III) and Mn(III) are the same (0.65 Å).<sup>55</sup> It was observed that even the preannealed samples (at 500 °C for 3 h) require temperatures as high as 650 °C to completely convert to the  $\alpha$  phase, indicating high activation energy for this process. The suppression of the cubic to hexagonal transition due to the free volume difference is the operational mechanism for the mixed oxide samples with an  $\text{Fe}_2\text{O}_3$  majority. However, the scenario changes when the Mn(III) concentration is more than 44 atom %. There, neither the  $\gamma$ - nor the  $\alpha\text{-Fe}_2\text{O}_3$  lattice can accommodate these mixed ion ratios, and the result is phase separation, as shown in Figure 5. For mixed oxide samples with a  $\text{Mn}_2\text{O}_3$  majority, that is, from 78 to 89 Mn(III) atom %, the  $\text{Mn}_2\text{O}_3$  structure prevails, because the Fe(III) ions are incorporated into the  $\text{Mn}_2\text{O}_3$  lattice, resulting in the  $\text{Mn}_{2-x}\text{Fe}_x\text{O}_3$  phase, where  $x = 0.22\text{--}0.44$ . The XRD pattern (Figure 4) supports this conclusion.

Having discussed the three regions in the mixed oxide phase diagram, we turn to a discussion of their magnetic properties. After all, control of composition and structure are meaningful *only* when control of properties is the result. We address these issues by magnetization measurements at different temperatures, corroborating these studies by measuring the spin density using EPR. Mössbauer spectroscopy will provide information of the oxidation state and specific site of the Fe(III) ions in the mixed

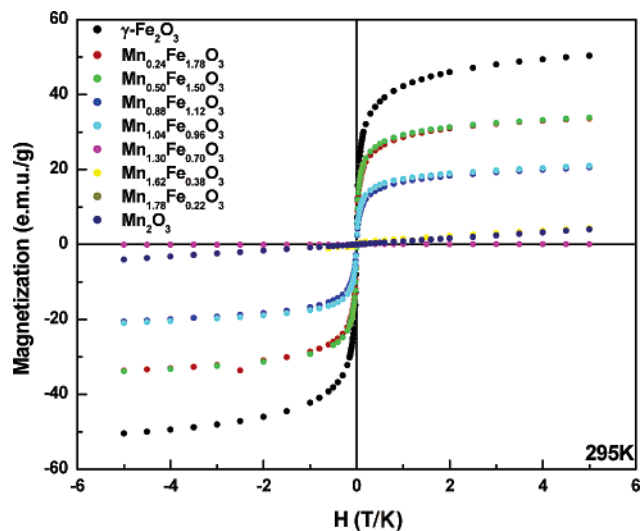


**Figure 6.** Magnetization curves at 295 K.

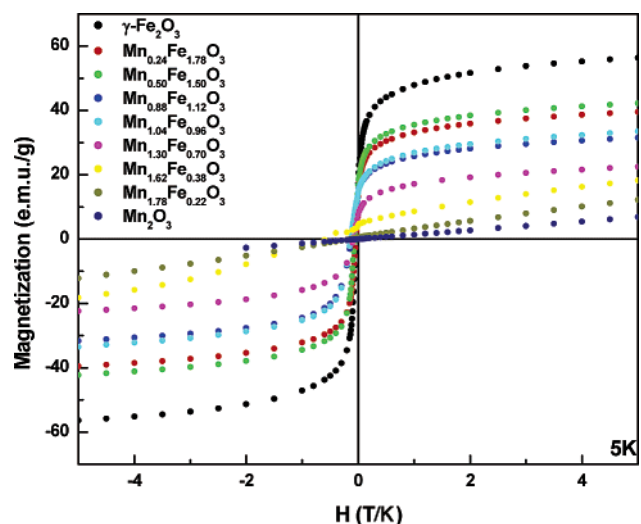


**Figure 7.** Magnetization curves at 5 K.

oxides, thus, allowing a deeper understanding of structure–property relationships.

Room temperature (295 K), as well as low temperature (5 K), magnetization curves of the oxides ( $\gamma\text{-Fe}_2\text{O}_3$ ,  $\text{Mn}_2\text{O}_3$ ) and mixed oxides ( $\text{Mn}_x\text{Fe}_{1-x}\text{O}_3$  ( $x = 0.12\text{--}0.89$ )) are presented in Figures 6 and 7, respectively. The magnetization curves of crystalline  $\gamma\text{-Fe}_2\text{O}_3$  and of mixed oxide nanoparticles with Mn(III) concentrations from 12 to 52 atom % show superparamagnetic behavior, with no coercivity at room temperature (bulk  $\gamma\text{-Fe}_2\text{O}_3$  is ferrimagnetic). On the other hand, the curves of  $\text{Mn}_2\text{O}_3$  and the mixed oxide samples with Mn(III) from 65 to 89 atom % are linear with small positive susceptibility, which is in agreement with the bulk  $\text{Mn}_2\text{O}_3$  antiferromagnetic behavior. The magnetic measurements are in accordance with XRD, showing the magnetic properties transforming from superparamagnetic to antiferromagnetic, as the crystal structure transforms from spinel to bixbyite. The lack of hysteresis, even at applied fields as high as 5 T, is an indication of single-domain nanoparticles.

ZFC and FC magnetic curves of the representative mixed oxide samples are shown in Figures 8 and 9. The broad nature of the ZFC curves indicates particle size distributions.<sup>56</sup> This may imply that some of the particles are not superparamagnetic anymore at room temperature and a nonequilibrium magnetization state for the ZFC case exists, which is confirmed by the

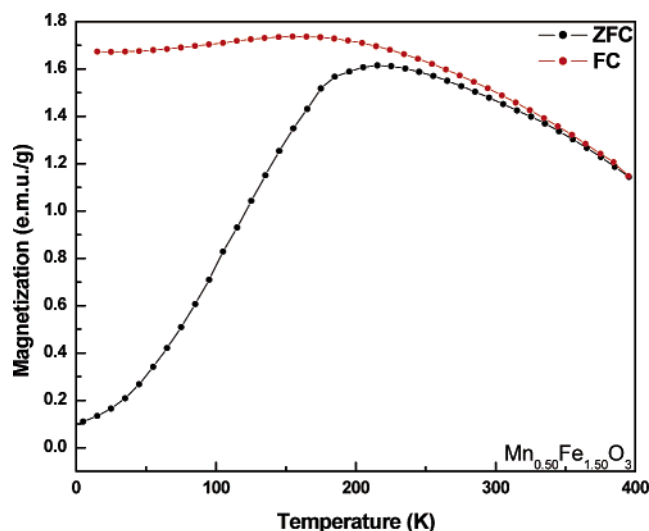


Figure 8. ZFC and FC curves of sample with 25% Mn(III).

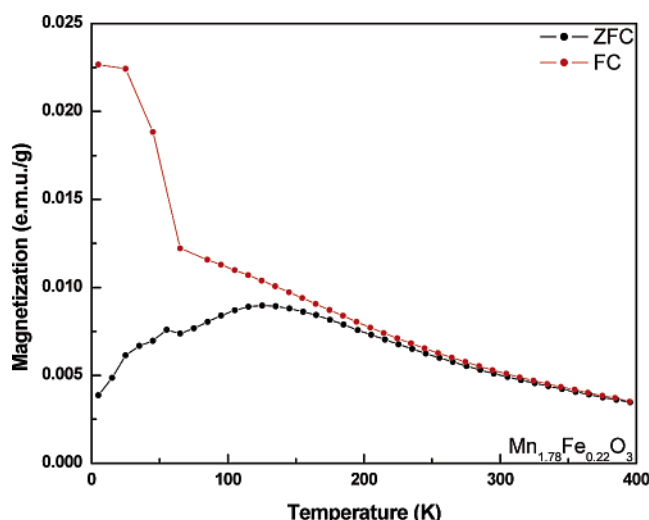


Figure 9. ZFC and FC curves of sample with 89% Mn(III).

fact that the ZFC and FC curves did not superimpose even if the measurements were done up to 400 K.

The Mössbauer spectrum of  $\gamma$ -Fe<sub>2</sub>O<sub>3</sub> (Supporting Information) shows 45% superparamagnetic behavior at room temperature (a doublet) and 55% ferrimagnetic contribution (sextuplet), with a distribution in the hyperfine field, due to a variety in particle size.<sup>57</sup> For the samples with 12 (Figure 10) and 78 atom % Mn(III) (Figure 11), the spectra are similar to those of the  $\gamma$ -Fe<sub>2</sub>O<sub>3</sub> with different ratios of the superpara-ferrimagnetic phases.

The Mössbauer parameters, that is, the isomer shifts and the quadrupole splitting for overall components of the samples, are in the range 0.3–0.5 and 0.8–0.9 mm/s, respectively. These values are in agreement with Fe<sup>3+</sup> ions in an octahedral environment. No Fe<sup>2+</sup> was detected, excluding the existence of any Fe<sub>3</sub>O<sub>4</sub> phase. The hyperfine field value shows distribution (due to size variation) with an average value of 490 kOe, which is lower than the bulk value (~514 kOe at room temperature), as a result of the size effect.<sup>57</sup> Additionally, the antiferromagnetic coupling between the Fe(III) and the Mn(III) sites might also reduce the value.

Having established that in all mixed oxide samples the iron is in the +3 oxidation state, we wanted to establish spin density in the different samples and find out if they correlate with the magnetic measurements. The studies reveal that the spin

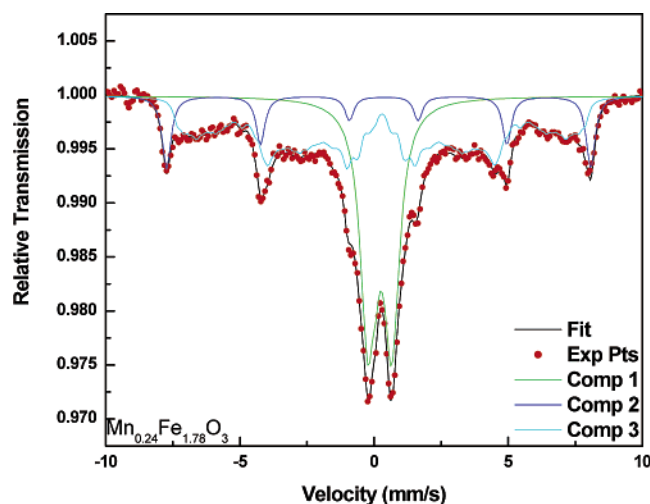


Figure 10. Mössbauer spectrum of a sample with 12% Mn(III) at 295 K.

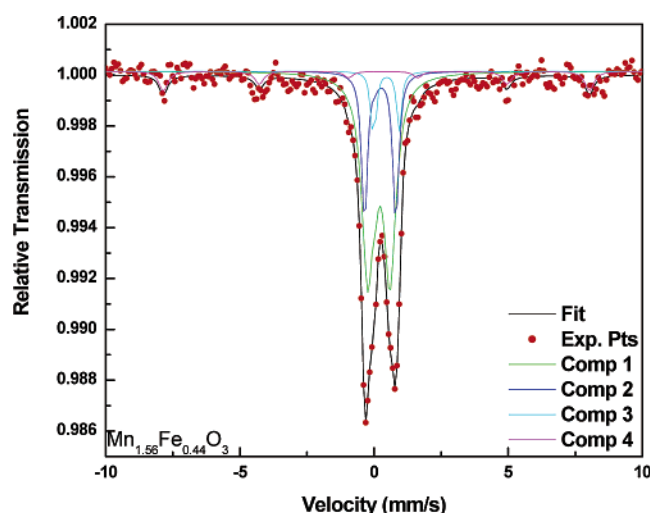
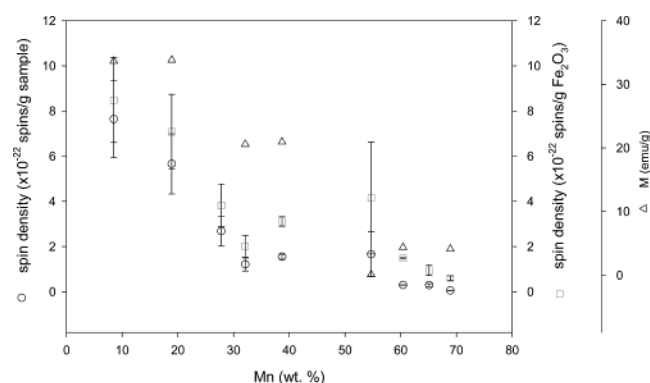
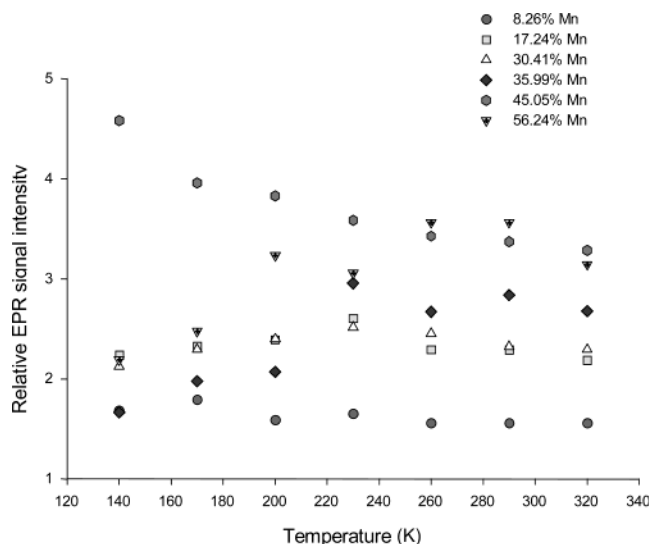


Figure 11. Mössbauer spectrum of sample with 78% Mn(III) at 295 K.

Figure 12. Spin density of manganese iron oxide based on per gram of sample (O) and per gram of Fe<sub>2</sub>O<sub>3</sub> (□) and magnetic moments (M, Δ) measured at 5 T versus weight percent of Mn (wt %).

densities (per gram of Fe<sub>2</sub>O<sub>3</sub> and per gram of sample) for Mn(III)-substituted Fe<sub>2</sub>O<sub>3</sub> nanoparticles decrease markedly with increasing Mn(III) concentration (Figure 12), as illustrated by magnetic studies. The spin density per gram of Fe<sub>2</sub>O<sub>3</sub> was obtained by dividing the spin density of the sample by the weight percent of Fe<sub>2</sub>O<sub>3</sub>. The normalized spin density of the sample with 89 atom %, that is, 61.85 wt %, Mn(III) is  $6 \times 10^{21}$  spins/g Fe<sub>2</sub>O<sub>3</sub>, 1 order of magnitude lower than that of the sample with



**Figure 13.** Variation of relative EPR signal intensity with temperature (intensity uncertainty:  $\pm 15\%$ ).

12 atom %, that is, 8.3 wt %, Mn(III) ( $8.5 \times 10^{22}$  spins/g  $\text{Fe}_2\text{O}_3$ ). Such a reduction in the normalized spin density can be attributed to antiferromagnetic coupling of Fe(III) with Mn(III). This observed efficient coupling suggests that most of the Mn(III) atoms are not located on the particle surface but enter into the bulk of the amorphous  $\text{Fe}_2\text{O}_3$  nanoparticles during ultrasonication, leading to a truly mixed oxide with close proximity of Mn(III) and Fe(III) ions, in fact, sharing the same lattice.

The normalized spin density decreases with increasing Mn(III) composition and levels off around 44 atom % (30.41 wt %) Mn(III), where Fe(III) and Mn(III) ions are present at an approximately equal ratio. At this level, increase in the Mn(III) concentration no longer creates efficiently more Fe(III)–Mn(III) pairs. At  $\sim 52$  atom % (35.99 wt %) Mn(III), one observes a slight increase in spin density, which continues to increase at 65 atom % (45.05 wt %) Mn(III), before decreasing again. This behavior can be justified by considering the two extreme cases first. Thus, doping  $\text{Fe}_2\text{O}_3$  with Mn(III) starts by replacing Fe(III) ions by Mn(III) ions in the  $\gamma\text{-Fe}_2\text{O}_3$  structure. Similarly, at the other end of the composition spectrum, doping  $\text{Mn}_2\text{O}_3$  with Fe(III) results in replacing Mn(III) by Fe(III) ions in the  $\text{Mn}_2\text{O}_3$  structure. However, in the middle Mn(III) concentration region [e.g., 52 and 65 atom % Mn(III)] it is no longer possible for a one-phase mixed oxide to exist, resulting in phase separation, with distinct  $\gamma\text{-Fe}_2\text{O}_3$  and  $\text{Mn}_2\text{O}_3$  domains. The presence of a ferrimagnetic phase,  $\gamma\text{-Fe}_2\text{O}_3$ , enhances the spin density. This is fully supported by XRD magnetic measurements.

The temperature dependence of the spin susceptibility varies with the Mn(III) concentration in the sample (Figure 13). None of the samples follows the Curie law in terms of increase in spin susceptibility with decrease in temperature. Only the sample with 65 atom % (45.05 wt %) Mn(III) exhibits a clear monotonic, but slow, increase in signal intensity with decrease in temperature. The fact that 65 atom % Mn(III) shows an increase in intensity with the decrease in temperature is yet another indication that it is a physical mixture of superparamagnetic  $\text{Fe}_2\text{O}_3$  and the antiferromagnetic  $\text{Mn}_{2-x}\text{Fe}_x\text{O}_3$  or  $\text{Mn}_2\text{O}_3$ .

The  $g$  values of  $\gamma\text{-Fe}_2\text{O}_3$  and  $\text{Mn}_2\text{O}_3$  were determined to be 2.214 and 2.135, respectively. With the increase of the Mn(III) concentration in the mixed oxide nanoparticles, the  $g$  value decreases from the higher  $g$  value of  $\gamma\text{-Fe}_2\text{O}_3$  toward a lower  $g$  value of  $\text{Mn}_2\text{O}_3$  (Figure 14), most likely due to exchange

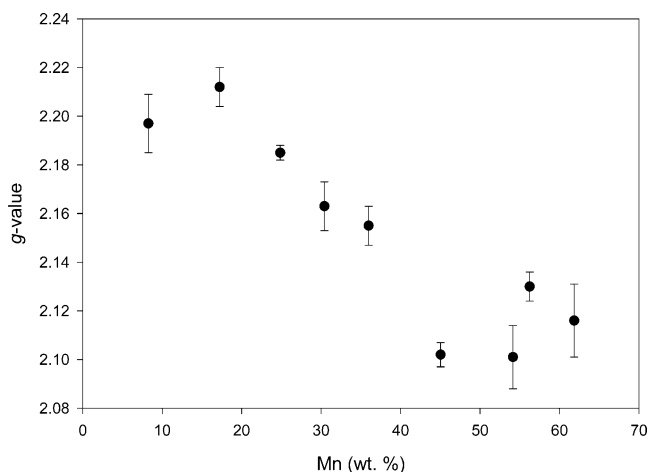


**Figure 14.** Room-temperature  $g$  value of manganese iron oxide with different compositions of Mn(III) wt %;  $g$ -value uncertainty is  $\pm 0.02$ .

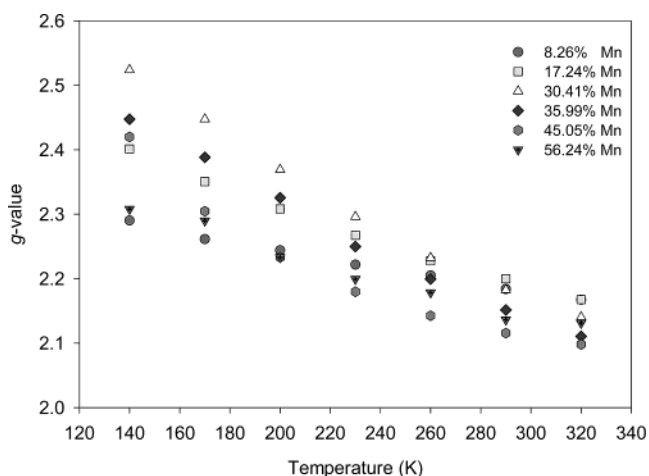


**Figure 15.** Temperature dependence of the  $g$  values of manganese iron oxide with different compositions of Mn(III) (wt %;  $g$ -value uncertainty is  $\pm 0.02$ ).

averaging. The  $g$  value of the samples increases with decreasing temperature (Figure 15). The nanoparticle sample with 44 atom % Mn(III) shows the highest slope with decreasing temperature, while that with the lowest Mn(III) doping (12 atom %) has the smallest temperature dependence. The  $g$  values for the 44 atom %, that is, 30.41 wt %, Mn(III) sample show the largest difference at room temperature and at 140 K (Figure 15).

The EPR signal for samples with Mn(III) content less than 44 atom % exhibits a Gaussian line shape. For samples above 44 atom % Mn(III), the inclusion of a larger Lorentzian component for higher Mn(III) content fits the line shapes better, indicating increasing exchange interaction with more Mn(III) incorporated.

At room temperature, the peak-to-peak line widths ( $\Delta H_{pp}$ ) do not show a strong dependence on the Mn(III) concentration (Figure 16). At 140 K, the  $\Delta H_{pp}$  are broader, as expected, as a result of lower averaging of the local field. The sample with 44 atom % (30.41 wt %) Mn(III) shows a marked change in line shape (Figure 17). The broadening of the line shape is because the measurement was carried out at temperatures lower than the blocking temperature for some nanoparticles. Notice that at 44 atom % Mn(III) concentration, the process of conversion of the manganese iron mixed oxide from spinel to bixbyite structure, just starts, leading to nonuniform local magnetic environments that can be further accentuated by lowering the temperature. At this junction, the behavior of EPR signals in

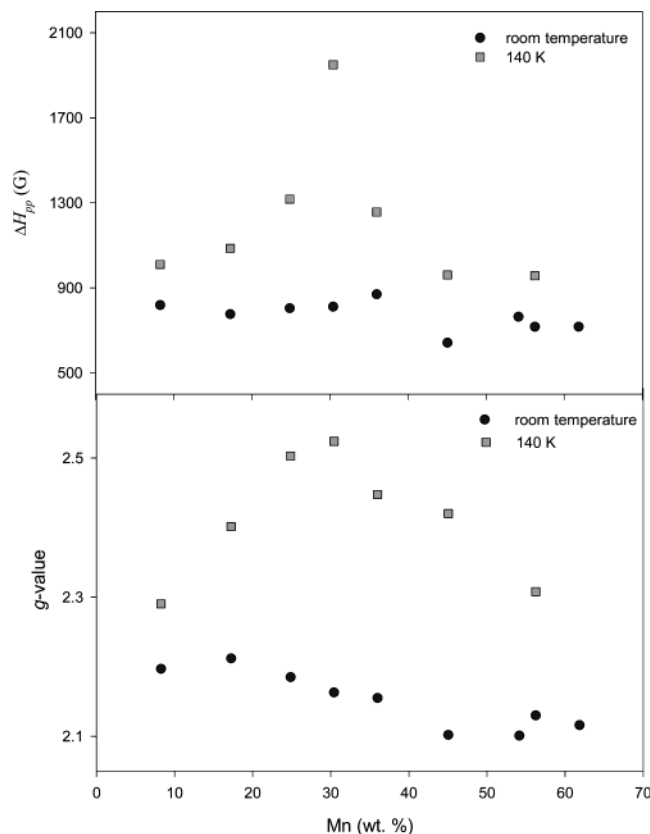


**Figure 16.** Peak-to-peak line width (upper curve) and  $g$  value (lower curve) at room temperature (●) and 140 K (■) with different weight percents of Mn(III) (line width uncertainty is  $<15$  G, depending on line shape).

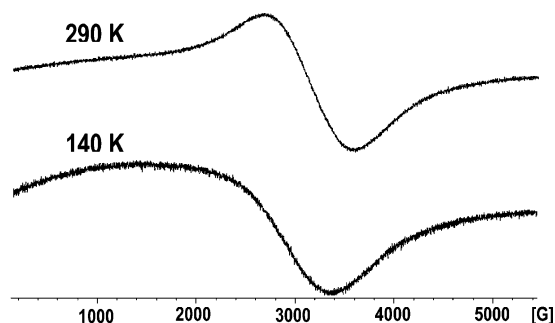


**Figure 17.** First-derivative EPR spectra of manganese iron mixed oxide with 44% Mn(III) at 290 and 140 K.

terms of spin density,  $g$  value, and line width all show significant changes in trend.

## Conclusions

We have presented detailed systematic studies of mixed iron–manganese oxide nanoparticles. All physical measurements suggest that ultrasonication of amorphous  $\text{Fe}_2\text{O}_3$  nanoparticles with  $\text{Mn}_2(\text{CO})_{10}$  provides complete mixing of the Fe(III) and Mn(III) ions in the amorphous mixed oxide samples. Depending on the mixed oxide composition, annealing results in either a one-phase or a phase-separated crystalline nanoparticle.

The results from XRD patterns, magnetization measurement, Mössbauer spectra, and EPR measurement can be summarized as follows. The XRD pattern reveals the structural progression from a  $\gamma\text{-Fe}_2\text{O}_3$ -like (spinel) to a  $\text{Mn}_2\text{O}_3$ -like (bixbyite) structure, with the increase in the Mn(III) concentrations. The  $\gamma\text{-Fe}_2\text{O}_3$  crystal structure of samples with low Mn(III) content shows

that the samples are single-phase compounds. This might be due to the replacement of Fe(III) atoms with Mn(III) atoms in the spinel lattice, as supported by EPR data of efficient antiferromagnetic coupling due to the presence Mn(III). This is corroborated by magnetization and EPR measurements where the systematic decrease in the magnetization as well the spin density values are observed. When the crystal structure is spinel, the magnetization measurement at room temperature shows superparamagnetism, and for the bixbyite structure, antiferromagnetism is observed. As for the samples with 65 atom % Mn(III), where the XRD patterns of samples show mixed phases of  $\text{Fe}_2\text{O}_3$  and  $\text{Mn}_{2-x}\text{Fe}_x\text{O}_3$ , the magnetization measurement shows antiferromagnetic behavior at room temperature, which changes to superparamagnetic upon cooling to 5 K. This confirms the presence of the ferrimagnetic component  $\text{Fe}_2\text{O}_3$  in the sample mixture. At 5 K, the ferromagnetic behavior is more pronounced and outweighs the antiferromagnetic component. When the temperature changes from room temperature to 77 K, the Mössbauer spectra of the same sample also changes from doublet to ferromagnetic sextuplet (Supporting Information). Thus, the results of magnetization measurement, Mössbauer spectra, and EPR measurement are also in close agreement.

**Acknowledgment.** This work was funded by the NSF through the MRSEC for Polymers at Engineered Interfaces. K.L. thanks the AvH Foundation for financial support. J.L. thanks the financial support from Robert Tsao Endowment Fellowship.

**Supporting Information Available:** Scheme showing the XRD setup at the X7B beamline of the National Synchrotron Light Source and Mössbauer spectrum of  $\gamma\text{-Fe}_2\text{O}_3$  at 295 K. This material is available free of charge via the Internet at <http://pubs.acs.org>.

## References and Notes

- (1) Shafi, K. V. P. M.; Ulman, A.; Yan, X.; Yang, N.-L.; Estournes, C.; White, H.; Rafailovich, M. *Langmuir* **2001**, *17*, 5093.
- (2) Brus, L. E. e. a. *J. Mater. Res.* **1989**, *4*, 104.
- (3) *Nanostructures and Quantum Effects*; Springer-Verlag: Berlin, 1997.
- (4) Woggon, U. *Optical Properties of Semiconductor Quantum*; Springer-Verlag: Berlin, 1997.
- (5) *Nanomagnetism*; Kluwer Academic Publishers: Dordrecht, The Netherlands, 1993.
- (6) *Magnetic Properties of Fine Particles*; North-Holland: Amsterdam, 1992.
- (7) *Science and Technology of Nanostructured Magnetic Materials*; Plenum Press: New York, 1991.
- (8) Audram, A. G.; Huguenard, A. P. U.S. Patent, 1981.
- (9) Ziolo, R. F. U.S. Patent, 1984.
- (10) McMichael, R. D.; Shull, R. D.; Swartzendruber, L. J.; Bennett, L. H.; Watson, R. E. *J. Magn. Magn. Mater.* **1992**, *111*, 29.
- (11) Pope, N. M.; Alsop, R. C.; Chang, Y.-A.; Sonith, A. K. *J. Biomed. Mater. Res.* **1994**, *28*, 449.
- (12) Marchessault, R. H.; Richard, S.; Rioux, P. *Carbohydr. Res.* **1992**, *224*, 133.
- (13) Josephson, L.; Tsung, C. H.; Moore, A.; Weissleder, R. *Bioconjugate Chem.* **1999**, *10*, 186.
- (14) Bhatnagar, S. P.; Rosensweig, R. E. *J. Magn. Magn. Mater.* **1995**, *149*.
- (15) Rosensweig, R. E. *Ferrohydrodynamics*; MIT Press: Cambridge, 1985.
- (16) Shafi, K. V. P. M.; Ulman, A.; Dyal, A.; Yan, X.; Yang, N.-L.; Estournes, C.; Fournes, L.; Wattaiaux, A.; White, H.; Rafailovich, M. *Chem. Mater.* **2002**, *14*, 1778.
- (17) Charles, S. W.; Popplewell, J. *Ferromagnetic Materials*; North-Holland: Amsterdam, 1980; Vol. 2.
- (18) Mehtha, R. V.; Upadhyay, R. V.; Dasanacharya, B. A.; Goyal, P. S.; Rao, K. S. *J. Magn. Magn. Mater.* **1994**, *132*, 153.
- (19) Kulikowski, J.; Lenniewski, A. *J. Magn. Magn. Mater.* **1980**, *19*, 117.



- (20) Long, J. W.; Qadir, L. R.; Stroud, R. M.; Rolison, D. R. *J. Phys. Chem. B* **2001**, *105*, 8712.
- (21) Ennas, G.; Marangiu, G.; Musinu, A.; Falqui, A.; Ballirano, P.; Caminiti, R. *J. Mater. Res.* **1999**, *14*, 1570.
- (22) Pascal, C.; Pascal, J. L.; Favier, F.; Moubtassim, M. L. E.; Payen, C. *Chem. Mater.* **1999**, *11*, 141.
- (23) Martinez, B.; Roig, A.; Molins, E.; Gonzalez-Carreno, T.; Serna, C. J. *J. Appl. Phys.* **1998**, *83*, 3256.
- (24) Morale, M. P.; Veintemillas-Verdaguer, S.; Serna, C. J. *J. Mater. Res.* **1999**, *14*, 3066.
- (25) Stober, W.; Fink, A.; Bohn, E. *J. Colloid Interface Sci.* **1968**, *26*, 62.
- (26) Jean, J. H.; Ring, T. A. *Langmuir* **1986**, *2*, 251.
- (27) Mounien, N.; Pileni, M. P. *Langmuir* **1997**, *13*, 3927.
- (28) Tang, B. Z.; Geng, Y.; Lam, J. W. Y.; Li, B.; Jing, X.; Wang, X.; Wang, F.; Pakhomov, A. B.; Zhang, X. X. *Chem. Mater.* **1999**, *11*, 1581.
- (29) Ziolo, R.; Giannelis, E. P.; Weinstein, B. A.; O'Horo, M. P.; Ganguly, B. N.; Mehrotra, V.; Russel, M. W.; Huffman, D. R. *Science* **1992**, *257*, 219.
- (30) Froba, M.; Kohn, R.; Bouffard, G. *Chem. Mater.* **1999**, *11*, 2858.
- (31) del Monte, F.; Morale, M. P.; Levy, D.; Fernandez, A.; Ocana, M.; Roig, A.; Molins, E.; O'Grady, K.; Serna, C. J. *Langmuir* **1997**, *13*, 3627.
- (32) Sui, Y.; Xu, D. P.; Zheng, F. L.; Su, W. H. *J. Appl. Phys.* **1996**, *80*, 719.
- (33) Morrish, A. H.; Haneda, K. *J. Appl. Phys.* **1981**, *52*, 2496.
- (34) Bee, A.; Massart, R.; Neveu, S. *J. Magn. Magn. Mater.* **1995**, *149*, 6.
- (35) Yu, H.-F.; Gadalla, A. M. *J. Mater. Res.* **1996**, *11*, 663.
- (36) Pannaparayil, T.; Marande, R.; Komarneni, S. *J. Appl. Phys.* **1991**, *69*, 5349.
- (37) Kodama, R. H.; Berkowitz, A. E.; McNiff, J. E. J.; Foner, S. *Phys. Rev. Lett.* **1996**, *77*, 394.
- (38) Shafi, K. V. P. M.; Koltypin, Y.; Gedanken, A.; Prozorov, R.; Balogh, J.; Lendvai, J.; Felner, I. *J. Phys. Chem. B* **1997**, *101*, 6409.
- (39) Kommareddi, N. S.; Tata, M.; John, V. T.; McPherson, G. L.; Herman, M. F.; Lee, Y.-S.; O'Connor, C. J.; Akkara, J. A.; Kaplan, D. L. *Chem. Mater.* **1996**, *8*, 801.
- (40) Mounien, N.; Veillet, P.; Pileni, M. P. *J. Magn. Magn. Mater.* **1995**, *149*, 67.
- (41) Suslick, K. S. *Science* **1990**, *247*, 1439.
- (42) Flint, E. B.; Suslick, K. S. *Science* **1991**, *253*, 1397.
- (43) Atchley, A. A.; Crum, L. A. *Ultrasound, its Chemical, Physical and Biological Effect*; VCH Press: New York, 1988.
- (44) Praserttham, P.; Silveston, P. L.; Mekasuwandumrong, O.; Pavarajarn, V.; Phungphadung, J.; Somrang, P. *Crys. Growth Des.* **2004**, *4*, 39.
- (45) Koltypin, Y.; Katabi, G.; Cao, X.; Prozorov, R.; Gedanken, A. *J. Non-Cryst. Solids* **1996**, *201*, 159.
- (46) Shafi, K. V. P. M.; Gedanken, A.; Goldfarb, R. B.; Felner, I. *J. Appl. Phys.* **1997**, *81*, 6901.
- (47) Cao, X.; Koltypin, Y.; Prozorov, R.; Felner, I.; Gedanken, A. *J. Mater. Chem.* **1997**, *7*, 1007.
- (48) Shafi, K. V. P. M.; Gedanken, A.; Prozorov, R.; Balogh, J. *Chem. Mater.* **1998**, *10*, 3445.
- (49) Koltypin, Y.; Cao, X.; Prozorov, R.; Balogh, J.; Kaptas, D.; Gedanken, A. *J. Mater. Chem.* **1997**, *7*, 2453.
- (50) Suslick, K. S.; Choe, S.-B.; Cichowlas, A. A.; Grinstaff, A. A. *Nature* **1991**, *353*, 414.
- (51) Grinstaff, M. W.; Salmon, M. B.; Suslick, K. S. *Phys. Rev. B* **1993**, *48*, 369.
- (52) Bellissent, R.; Galli, G.; Hyeon, T.; Magazu, S.; Majolino, D.; Migliardo, P.; Suslick, K. S. *Phys. Scr., T* **1995**, *57*, 79.
- (53) Smith, G. C. *Synchrotron Radiat. News* **1991**, *4*, 24.
- (54) Lai, J.; Shafi, K. V. P. M.; Loos, K.; Ulman, A.; Lee, Y.; Vogt, T.; Estournès, C. *J. Am. Chem. Soc.* **2003**, *125* (38), 11470.
- (55) Snider, B. B. *Chem. Rev.* **1996**, *96*, 339.
- (56) Dyal, A.; Loos, K.; Noto, M.; Chang, S. W.; Spagnoli, C.; Shafi, K. V. P. M.; Ulman, A.; Cowman, M.; Gross, R. *J. Am. Chem. Soc.* **2003**, *125*, 1684.
- (57) Shannon, R. D.; Prewitt, C. T. *Acta Crystallogr.* **1970**, *B42*, 1076.
- (58) Morup, S. *Europhys. Lett.* **1994**, *28*, 671.
- (59) Shafi, K. V. P. M.; Ulman, A.; Dyal, A.; Yan, X.; Yang, N.-L.; Estournès, C.; Fournes, L.; Wattiaux, A.; White, H.; Rafailovich, M. *Chem. Mater.* **2002**, *14*, 1778.